

Impact of Topographic Wind Conditions on Dust Particle Size Distribution: Insights from a Regional Dust Reanalysis Dataset

Xinyue Huang¹, Wenyu Gao², Hosein Foroutan¹

¹Department of Civil and Environmental Engineering, Virginia Tech, Blacksburg, VA, 24060, USA

²Department of Mathematics and Statistics, University of North Carolina at Charlotte, Charlotte, NC, 28223, USA

Correspondence to: Hosein Foroutan (hosein@vt.edu)

Abstract. The size of windblown dust particles plays a critical role in determining their geochemical and climate impacts. This study investigates the relationship between topographic wind conditions (speed and direction relative to land slope) and the particle size distribution of dust emissions on a regional scale. We used the Multiscale Online Nonhydrostatic Atmosphere Chemistry (MONARCH) dust reanalysis dataset, which assimilates satellite data on coarse-mode dust optical depth (DOD_{coarse}). Validation against flight measurements from the 2011 Fennec campaign confirms the reanalysis's effectiveness in capturing coarse to super coarse dust. A 10-year dust reanalysis underwent selective screening to identify events with fresh emissions and the fraction of coarse dust concentrations was calculated as a surrogate for size distribution. The coarse fractions and associated meteorological and land characteristics obtained from various datasets were incorporated into multiple linear regression and machine learning models. Results indicate that dust particle size increases with wind speed, likely due to a higher fraction of fresh emissions and reduced deposition of coarse dust under stronger winds. A positive correlation between dust size and uphill slope suggests that enhanced vertical transport of dust by topography outweighs the impact of shifting emission microphysics over veering winds. Both positive correlations weaken in the afternoons and summer, likely due to the turbulence during haboob storms, which can suspend coarse dust from aged emissions, competing with the effect of uphill slopes. These findings on dust size dependency on topographic winds could improve dust cycle representation and its impacts.

1 Introduction

Windblown dust particles emitted from arid and semi-arid areas are the largest terrestrial contributor to global aerosols (Brasseur and Jacob, 2017). Understanding the size of the airborne dust particles is crucial for assessing their impacts on global climate and biogeochemistry. Size plays an important role in determining the emission and deposition of dust particles and thus the redistribution of soil nutrients around the globe (Knippertz, 2017; Duce and Tindale, 1991; Wang et al., 2023). Additionally, particle size can affect the likelihood of microorganisms' attachment to dust aerosols (Polymenakou et al., 2008; Yamaguchi et al., 2012) and the distance these associated microorganisms can travel (Prospero et al., 2005; Kellogg and Griffin, 2006). Particle size, along with other factors such as mineralogy, chemical composition, and shape, controls the climate

33 impacts of dust particles which can vary drastically from warming to cooling (Adebiyi and Kok, 2020; Kok et al., 2023;
34 Mahowald et al., 2014). Realistic representation of dust particle size distribution (PSD) in the atmosphere requires an
35 understanding of the dependencies of dust size at emission (Kok, 2011; Rosenberg et al., 2014).

36 Relationships between dust PSD and various environmental factors have been extensively studied. Soil moisture has been
37 widely reported to increase the proportion of coarse dust in emissions by enhancing bonding forces among fine particles within
38 soil aggregates (Dupont, 2022; González-Flórez et al., 2023; Shao et al., 2020), but one recent study also argues that the effect
39 is non-monotonic (Ma et al., 2023). Another surface characteristic of interest is soil texture. Emitted dust PSD during wind
40 tunnel experiments was reported to be significantly influenced by the fully dispersed soil size distribution (Wang et al., 2021),
41 and proportion of emitted submicron particles and PM_{10} increased after tillage practices which broke down soil aggregates
42 (Fernandes et al., 2023; Katra, 2020). The effect of atmospheric stability on dust size is inconsistent across studies. Some
43 reported that an unstable atmospheric boundary is associated with richer submicron particles (Khalfallah et al., 2020; Shao et
44 al., 2020), whereas others found no effect (Dupont, 2022; González-Flórez et al., 2023). Deposition impacts are universally
45 acknowledged and were evaluated using characteristics of dust events or dust measurements, including fetch length (González-
46 Flórez et al., 2023), dust age (Dupont et al., 2015; Ryder et al., 2013), and dust measurement height (Khalfallah et al., 2020;
47 Shao et al., 2020). Nevertheless, the effects of multiple factors often intertwine during dust events, making the overall impact
48 on dust size obscure.

49 Wind speed, or the resulting friction velocity (u_*) exerted on the ground surface, as the driving force of dust emissions, is one
50 of the most essential parameters for dust emissions. The relationship between wind speed and PSD of dust emissions has been
51 widely studied, yet consensus is lacking. Saltation-bombardment and aggregate disintegration are usually considered the
52 primary mechanism for dust emissions (Kok et al., 2012). Parametrization of saltation-bombardment proposed that higher u_*
53 leads to higher energy in saltating particles and thus enhances the breaking down of soil aggregates and ejection of fine particles
54 (Shao, 2001). This theory is supported by multiple wind tunnel experiments (Alfaro et al., 2022; Wang et al., 2021) and field
55 measurements (Chkhietiani et al., 2021; Dupont, 2022; Khalfallah et al., 2020). The brittle fragmentation theory, on the other
56 hand, postulates that PSD of vertical dust flux is independent of u_* , backed by compiled data from multiple wind tunnel and
57 field measurements (Kok, 2011). Some also proposed that detachment of submicron particles from the surface of soil
58 aggregates is more common when kinetic energy of impacting particles is low and the ejection of coarser particle from
59 fragmentation becomes increasingly dominant with higher impaction intensity (Malinovskaya et al., 2021). These
60 discrepancies are partially due to the interplay of other factors, such as inconsistencies in dust emission measurements
61 (Khalfallah et al., 2020; Shao et al., 2020), soil moisture (Ishizuka et al., 2008; Shao et al., 2020; Webb et al., 2021), and
62 whether steady state saltation is reached (Mahowald et al., 2014). Selection of the dust emission properties (e.g., dust flux or
63 dust concentration; Shao et al., 2020) and the height of dust measurements (Khalfallah et al., 2020) can alter the dust PSD.
64 The effects of soil moisture on shifting dust PSD at emission can get entangled with the potential effects of u_* . For instance,
65 the fine fraction in dust emissions counterintuitively increasing with decreasing u_* after light rain was caused by drying of the

66 weakly crusted soils over time (Shao et al., 2020). With interferences of various factors, predicting the general dependency of
67 PSD of dust emission on u_* at regional scales over longer time becomes complex.

68 The role of topography in altering size of dust emission is of emerging interest. The orographic channelling of winds can affect
69 the dust emission or transport (Caton Harrison et al., 2021; Rosenberg et al., 2014). Uphill winds can enhance the vertical
70 transport of dust particles through flow separation, especially increase the proportion of coarse particles in the elevated dust
71 based on computational simulations (Heisel et al., 2021). Moreover, the veering angle between wind vectors and the surface
72 inclination can affect the emitted dust PSD. A study over a local field observed that compared to winds that blew more parallel
73 to the ridges of the slopes (i.e., tangential winds), frontal uphill winds generated a higher fraction of fine particles (0.2-2 μm)
74 because of more sputtering of fine particles on the windward slope due to resistance from the secondary aeolian structures, as
75 well as less generation of coarse particles (2-5 μm) on the leeward slope with the recirculation zone (Malinovskaya et al.,
76 2021). Other potential topographic impacts include the generation of erodible material by certain orographic winds
77 (Washington et al., 2006) and the triggering of convective storms by mountains (Knippertz et al., 2007). However, their
78 associations with dust PSD are understudied. Overall, it remains unclear whether the observed effects of wind over local
79 topography on the PSD of dust emissions is detectable at regional scales and what the overall relationship between topography
80 and dust PSD will be.

81 Understanding the relationship between topographic wind conditions and PSD of dust emission on a regional scale is important
82 for simulating dust activities and impacts in atmospheric or climate models. Complementing the accumulating field data on
83 PSD of dust emissions (Shao et al., 2020; González-Flórez et al., 2023; Fernandes et al., 2023), this study aims to explore the
84 impacts of topographic wind conditions on dust PSD on a regional scale through data analysis. The regional scale means that
85 the dust emission of concern inevitably includes near-source transport and deposition. Here, we selected “fresh” dust emission
86 events from the Multiscale Online Nonhydrostatic AtmospheRe Chemistry model (MONARCH) dust reanalysis data (Di
87 Tomaso et al., 2022) and constructed models to investigate the correlations between PSD of surface dust concentrations in
88 fresh emissions and wind conditions over slopes, while taking into account other relevant meteorological and surface
89 conditions. Our methodology, sensitivity analysis, and evaluations are described in Section 2, and the discussion of our findings
90 followed by the main takeaways are presented in Sections 3 and 4.

91

92 **2 Data and Methods**

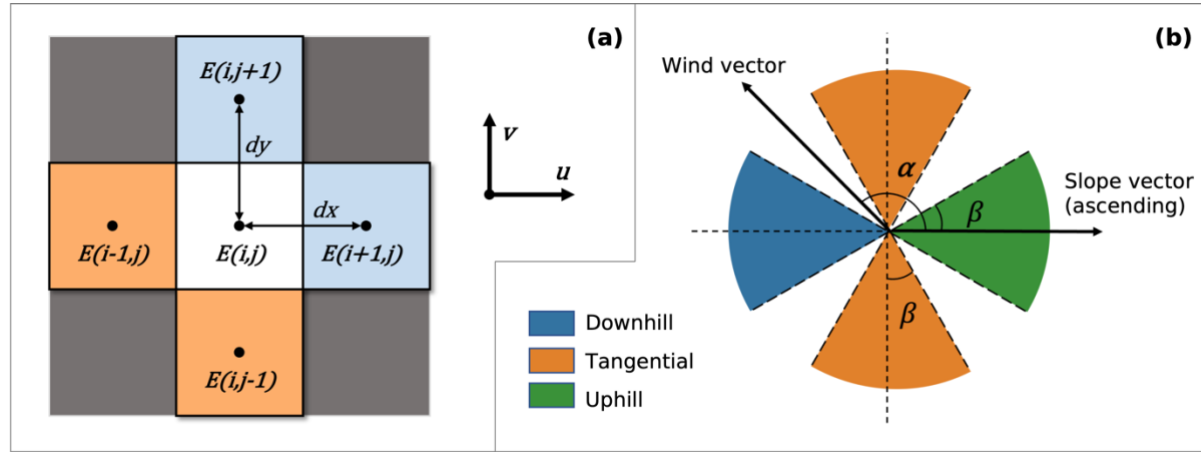
93 **2.1 Datasets and variables**

94 The study domain (12-38° N, 18W-36° E) encompasses the Sahara Desert, the largest dust source on Earth, which contributes
95 to around 60% of the global dust loading (Tanaka and Chiba, 2006). Various monitoring or reanalysis datasets are available
96 for this region, providing information on African dust sizes and the associated environmental conditions needed for this study.

97 The Multiscale Online Nonhydrostatic AtmosphRe Chemistry model (MONARCH) dust reanalysis (Di Tomaso et al., 2022)
98 dataset provides size-resolved dust information from 2007 to 2016 with 3-hour intervals. The dataset covers North Africa, the
99 Middle East, and Europe using a rotated-pole projection with a spatial resolution of 0.1° . The assimilation data of coarse-mode
100 dust optical depth (DOD_{coarse}) were derived from the Moderate Resolution Imaging Spectroradiometer (MODIS)-Aqua Deep
101 Blue level 2 aerosol products (Collection 6), including aerosol optical depth (AOD), the Ångström exponent, and the single
102 scattering albedo at different wavelengths (Ginoux et al., 2012; Pu and Ginoux, 2016). MONARCH's first-guess dust size
103 distribution follows the brittle-fragmentation theory of Kok (2011) with perturbations across 12 ensemble members. By
104 applying a local ensemble transform Kalman filter with four-dimensional extension (4D-LETKF) at each 24-hour assimilation
105 window, reanalysis increments were added to the model ensemble simulations (first-guess) to match the DOD_{coarse}
106 observations. Specifically, the dust state vector of the total coarse dust mixing ratio (distributed across five coarser bins from
107 1.2 to $20\text{ }\mu\text{m}$) was updated, then the increments for the finer three bins were determined proportionally to their total relative
108 mass. Therefore, although MONARCH reanalysis does not directly assimilate fine-mode DOD, corrections in the coarse bins
109 propagated to the entire PSD through the assimilation state vector and physical parameterizations, aligning the PSD more
110 closely with dust-specific observations. Consequently, if the prior PSD is biased—for instance by placing too much mass in
111 the largest bin or not enough in a medium bin—that bias may persist to some extent after assimilation. Despite the limitation,
112 validation against AERONET data indicates that fine dust is still captured satisfactorily (Di Tomaso et al., 2021; Mytilinaios
113 et al., 2023), supporting the reliability of the dataset to investigate dust PSD. We hypothesize that the dust concentration
114 reanalysis captures the potential regional effects of topographic wind conditions on the dust PSD via assimilation of the satellite
115 DOD_{coarse} observations. The adjustments in dust concentration PSD during data assimilation were showcased by the uneven
116 ratio of the first-guess dust concentration to its reanalysis across eight size bins (see section 2.2 and Fig. S1). The MONARCH
117 model was run in 40 hybrid pressure-sigma model layers and the dust concentration in the lowest layer is saved as the surface
118 dust concentration. The surface dust concentration best represents near-source dust emissions and transport, and was chosen
119 for this study. The concentration is available in eight size bins (i.e., $0.2\text{--}0.36$, $0.36\text{--}0.6$, $0.6\text{--}1.2$, $1.2\text{--}2.0$, $2.0\text{--}3.6$, $3.6\text{--}6.0$, 6.0--
120 12.0 , and $12.0\text{--}20.0\text{ }\mu\text{m}$; Klose et al., 2021)). For easier comparison, these size-resolved concentrations were condensed into
121 a single index called the “coarse fraction”, defined as the sum of mass concentrations of the coarsest two bins ($6\text{--}12\text{ }\mu\text{m}$)
122 divided by the total mass concentration of all eight bins (referred to as “cf2”). The delineation of fine and coarse particles is
123 somewhat arbitrary and case-specific across studies. In general, a cutoff diameter from submicron to above $10\text{ }\mu\text{m}$ was used
124 (Dupont, 2022; Fernandes et al., 2023; Panebianco et al., 2023) and the most common range is roughly $2\text{--}5\text{ }\mu\text{m}$ (Ishizuka et
125 al., 2008; Ryder et al., 2019; Shao et al., 2020; Webb et al., 2021), which generally aligns with the lower boundary of $6\text{ }\mu\text{m}$
126 used in this study. Additionally, we tested alternative definitions of coarse fraction (namely “cf1” and “cf3”, where the coarsest
127 one or three bins are assigned as coarse dust) in the subsequent statistical analysis and results suggest that cf2 is a representative
128 surrogate for dust particle size. More details on the comparison are included in Table S4 and Section 3.3.

129 Because wind conditions associated with dust concentrations are not available from the MONARCH dust reanalysis dataset,
 130 we sourced the information from the Modern-Era Retrospective analysis for Research and Applications (MERRA-2) data
 131 (Gelaro et al., 2017). MONARCH ensemble simulations applied meteorological inputs from two reanalysis datasets, i.e.,
 132 MERRA-2 and ERA-Interim. Given that wind from both reanalyses are highly constrained by observations, and there is a
 133 substantial overlap in the assimilated data used by the two (Fujiwara et al., 2024; Rienecker et al, 2008; Dee et al., 2011; Gelaro
 134 et al., 2017), it is reasonable to use MERRA-2 wind vectors to inform the wind conditions of MONARCH dust reanalysis.
 135 The available wind components nearest to the surface and most relevant to dust emissions are at 2 meters above ground,
 136 provided as hourly average with a spatial resolution of 0.5° latitude $\times 0.625^\circ$ longitude in the product M2I1NXASM. Wind
 137 speed and wind direction are subsequently calculated.

138



139

140 **Figure 1.** (a) Variables used in the calculation of upwind slope. The elevations in the target grid, $E(i,j)$ and the upwind grids (in orange if
 141 the wind components were positive; in light blue if the wind components were negative) were used to calculate the upwind slope components
 142 in x and y directions. (b) Methods for assigning the type of wind direction over topography. The angle between the upwind slope and the
 143 wind vector, α , and the predefined cut-off angle, β , together determine whether the wind from an event is typical for any of the three
 144 categories of relative wind direction, namely downhill, tangential, and uphill winds.

145

146 The wind direction types relative to topography (hereafter “relative wind direction type”) were determined based on the angle,
 147 α ($0 \leq \alpha < 360^\circ$) between the wind vector ($u(i,j)$ and $v(i,j)$) and the slope vector ($S_x(i,j)$ and $S_y(i,j)$). Elevation data for calculating
 148 the slope were retrieved from the NASA Shuttle Radar Topography Mission Global 3 arc-second (SRTM GL3) dataset (Farr
 149 et al., 2007). The SRTM elevation data are expected to be compatible with the MERRA-2 wind reanalysis because 1) both the
 150 SRTM and GTOPO30, which is used in the Goddard Earth Observing System (GEOS-5) model (MERRA-2’s first-guess),
 151 have much finer than MERRA-2’s grid, making their spatial averages comparable, and 2) MERRA-2 wind reanalysis are
 152 highly constrained by assimilated observations, reducing its dependency on topographic input. Dust concentration is most
 153 relevant to emissions in upwind grids, therefore, slope vector components in each grid (i,j) were determined as gradients of

154 elevation between the target grid and the two neighboring grids in the upwind directions (Fig. 1(a) & Eq. (1)). To the best of
155 the authors' knowledge, this study presents the first derivation of the upwind slope over North Africa.

156 The wind direction over topography was categorized into tangential, uphill, and downhill winds depending on the angle α
157 between the slope and wind vectors as well as a predefined cut-off angle, β ($0 < \beta \leq 45^\circ$) (Fig. 1(b) & Eq. (2)). A smaller cut-
158 off angle results in a more selective process for assigning the relative wind direction types.

159

$$160 \quad S_x(i,j) = \begin{cases} \frac{E(i,j) - E(i-1,j)}{dx}, & u(i,j) > 0 \\ \frac{E(i,j) - E(i+1,j)}{dx}, & u(i,j) < 0 \end{cases}, \quad S_y(i,j) = \begin{cases} \frac{E(i,j) - E(i,j-1)}{dy}, & v(i,j) > 0 \\ \frac{E(i,j) - E(i,j+1)}{dy}, & v(i,j) < 0 \end{cases}, \quad (1)$$

161

162 where (i,j) denotes the location of a grid cell, $E(i,j)$ represents the elevation, and $S_x(i,j)$ and $S_y(i,j)$ represent the slope
163 components in x and y directions, respectively. The $u(i,j)$ and $v(i,j)$ are horizontal wind components.

$$164 \quad \text{wind type} = \begin{cases} \text{uphill,} & 0 < \alpha < \beta \text{ or } (360^\circ - \beta) < \alpha < 360^\circ \\ \text{tangential,} & (90^\circ - \beta) < \alpha < (90^\circ + \beta) \text{ or } (270^\circ - \beta) < \alpha < (270^\circ + \beta), \\ \text{downhill,} & (180^\circ - \beta) < \alpha < (180^\circ + \beta) \end{cases}, \quad (2)$$

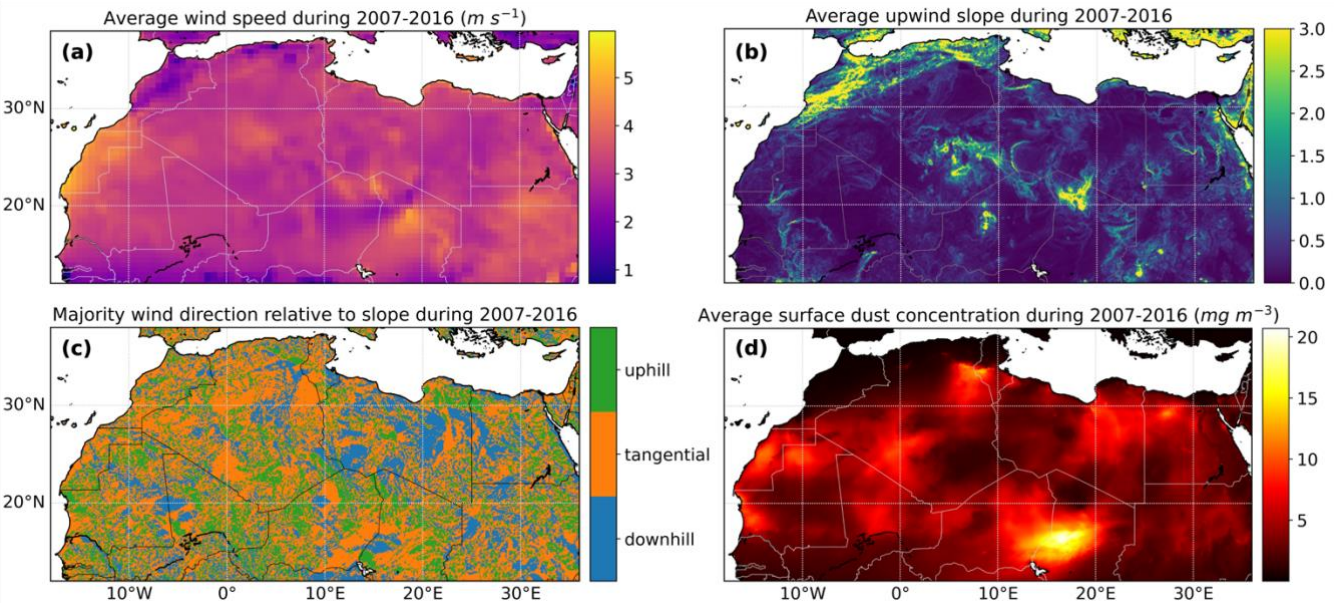
165

166 The land characteristics of soil texture and soil moisture that are expected to cast impacts on PSD of dust emissions were
167 considered. Spatial distribution of soil texture was adopted from the map used in the Global Land Data Assimilation System
168 version 2 (GLDAS2) Noah land surface model (Rodell et al., 2004), derived from the global soil dataset by Reynolds et al.
169 (2000). The texture of the top layer of soil was categorized into the 16 classes developed by the Food and Agricultural
170 Organization (FAO), varying in sand, silt, and clay fractions (Jahn et al., 2006). Soil moisture data were retrieved from the
171 MERRA-2 product M2T1NXLND, providing average water content in the top 5-centimeter layer of soil hourly with a spatial
172 resolution of 0.5° latitude $\times 0.625^\circ$ longitude.

173 All datasets were co-registered onto a universal 0.1° Plate Carrée coordinate. MERRA-2 and MONARCH data were regridded
174 using the Python xesmf package version 0.7.1 (Zhuang et al., 2023). The 2 m wind vectors and the soil moisture from the
175 MERRA-2 reanalysis underwent upsampling using the “nearest source to destination” algorithm to match MONARCH’s finer
176 resolution. This algorithm does not bring in artificial variations so is the safest choice for regridding. Coarser spatial resolution
177 of the MERRA-2 data means some neighboring grids will inevitably share the same wind vector and soil moisture, diminishing
178 the potential effects of wind conditions on dust PSD. The SRTM elevation data with a much higher original resolution were
179 downsampled using the “average” method provided by the Python package of geowombat version 2.1.6 (Graesser, 2023). Sub-
180 grid information on topography was lost, but handling topography information at the same scale as the wind data is reasonable

181 because the terrain variations at finer resolution are deemed smooth when scaling up. Soil texture data at 0.25° lat-lon
 182 coordinates were also projected to the 0.1° coordinates. To match the instantaneous 3-hourly timesteps of the MONARCH
 183 reanalysis, we picked the average wind components and soil moisture from the precedent hour, relevant to the initial dust
 184 emissions that can remain airborne during that period. Maps showing the average wind speed, the average upwind slope, the
 185 most common wind direction types, and the average surface dust concentration at 0.1° resolution over the 10 years are
 186 presented in Fig. 2. While we acknowledge the inherent resolution limitations of reanalysis datasets, the focus of this study is
 187 on the broader-scale modulation of dust emission by wind conditions, and data assimilation combined with upsampling
 188 techniques ensure that our conclusion remain interpretable in this context.

189



190

191 **Figure 2.** General spatial patterns of (a) 2-m wind speed from the MERRA-2 reanalysis, (b) calculated upwind slope, (c) derived wind
 192 direction type relative to slope using cut-off angle of 10° , and (d) MONARCH total dust concentration at ground surface from 2007 to 2016.
 193 The average values are shown for wind speed, upwind slope, and dust surface concentration, and the most frequent types are shown for the
 194 relative wind direction.

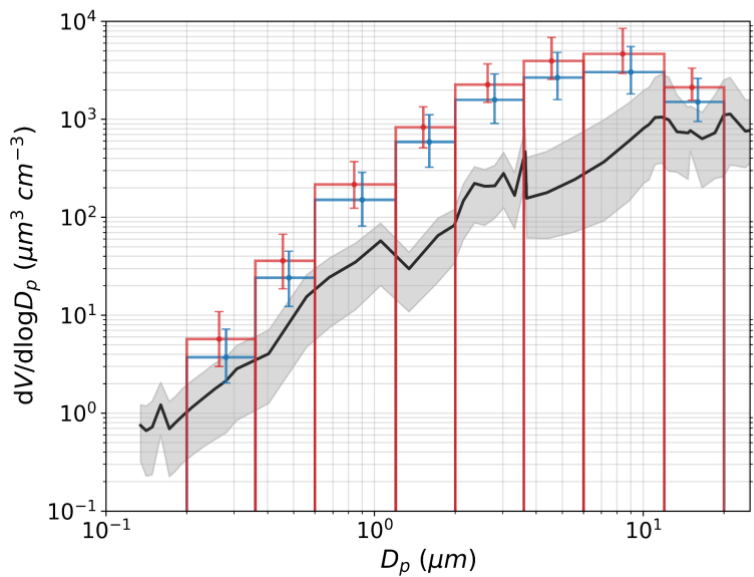
195

196 2.2 Validation against the Fennec measurements

197 The MONARCH dust reanalysis dataset was previously evaluated against observations from the Aerosol Robotic Network
 198 (AERONET) retrievals (Di Tomaso et al., 2021; Mytillinaios et al., 2023). Comparison between the 3-hourly MONARCH
 199 reanalysis of DOD_{coarse} at 550 nm and the coarse-mode AOD at 500 nm from AERONET retrievals over Sahara generate a
 200 Pearson correlation of 0.81 with a root mean square error of 0.15 (Di Tomaso et al., 2022). Here, we present an additional case

201 study to particularly evaluate the performance of dust reanalysis on capturing fresh dust emissions. Observational data were
 202 obtained from the 2011 Fennec campaign, where size-resolved dust emissions over western Africa were intensively sampled
 203 using wing-mounted instruments (Ryder et al., 2013). Segments of three flights (b600–602), each lasted 10 minutes, over
 204 northern Mali on 17–18 June 2011, were identified to be associated with fresh dust uplifts by low-level jets (Ryder et al., 2013;
 205 Ryder et al., 2015). Measured dust number concentration during these flight segments was converted to volumetric
 206 concentration for easier comparison with the MONARCH reanalysis data. The MONARCH reanalysis grids containing any
 207 portion of these flight trajectories were identified, and the associated dust mass concentrations were retrieved. These
 208 concentrations were weighted averaged by flight duration in each grid cell to yield an overall binned dust concentration. The
 209 MONARCH dust mass concentrations were also converted into volumetric concentrations using the dust particle density of
 210 2500 kg m⁻³ for the finer four bins and 2,650 kg m⁻³ for the coarser four bins (Klose et al., 2021). As shown in Fig. 3, the trends
 211 of two dust PSDs generally agree well across all the eight size bins of the MONARCH dataset. Most notably, MONARCH
 212 reanalysis is effective at capturing the coarse to super coarse modes (defined as dust with diameter greater than 10 µm; Meng
 213 et al., 2022) represented by the last three bins (3.6–20 µm), outperforming several recent dust simulations that lack the data
 214 assimilation (Adebiyi and Kok, 2020; Meng et al., 2022). Additional investigations (see Fig. S1) revealed that the reanalysis
 215 dust concentration changes non-monotonically from its first-guess, leading to the conclusion that not only the total dust
 216 concentration but also its PSD has changed due to assimilation. Overall, the predicted concentration for fresh emitted dust lies
 217 in an acceptable range, and the data assimilation process improved concentration across all bins as well as adjusted the dust
 218 size distribution, suggesting that the MONARCH reanalysis reasonably represents fresh dust emissions.

219



220

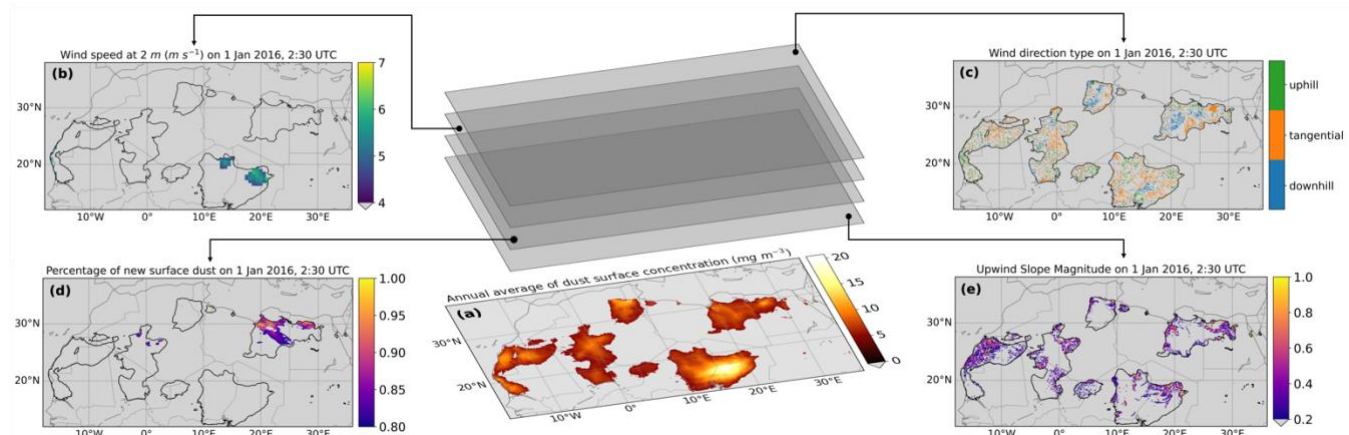
221 **Figure 3.** The black line shows the average volumetric concentration ($\mu\text{m}^3 \text{ cm}^{-3}$) of dust sampled during three Fennec flights (6 flight
 222 segments) and the grey shaded area denotes the range of values. The blue bars show the volumetric concentration ($\mu\text{m}^3 \text{ cm}^{-3}$) of dust in
 223 corresponding grids from the MONARCH reanalysis calculated from the weighted average mass concentration, with a particle density of
 224 2,500 kg m^{-3} for the finer four bins and 2,650 kg m^{-3} for the coarser four bins. The error bars denote the range of values.

226 2.3 Event selection and sensitivity tests

227 Addressing the specific goals of this study requires the selection of the most relevant dust events from a decade of data over
 228 northern Africa. Two goals guided the screening process: 1) excluding the aged dust, and 2) focusing on wind conditions over
 229 distinctive terrain variations. Several screening criteria were accordingly developed that must be met simultaneously for dust
 230 events to be eligible for further analysis. Specifically, the selected dust events must occur within dust sources and over terrain
 231 with prominent slopes, be concurrent with high wind speeds and typical wind directions over slope, and have notable increases
 232 in dust surface concentrations. The procedures for screening these events are illustrated in Fig. 4 and described below in detail.
 233 This highly selective approach was made possible by the abundance of data from the MONARCH reanalysis.

234 To start with, dust events were confined to dust sources to exclude long-range transported and likely aged dust far from dust-
 235 source regions. The 10-year average of surface dust concentrations was calculated for the entire study domain, and pixels with
 236 values above the threshold percentile were designated as dust sources. For example, dust sources selected using the 80th
 237 percentile of the 10-year average dust concentration as the threshold are presented in Fig. 4(a). The map of dust sources features
 238 the Bodélé Depression, Great Sand Sea, Tanezrouft, and the Atlantic Coastal Desert, consistent with the dust sources identified
 239 in other studies (Formenti et al., 2011; Di Tomaso et al., 2022). Further screening steps were performed independently within
 240 these dust sources.

241



242 **Figure 4.** Schematics showing the procedures for screening the 10-year dust reanalysis data for fresh dust emissions. First, dust sources were
 243 assigned to regions where the annual average of dust surface concentration is among the top percentile (i.e., 20% as shown in (a)) of all
 244 values across the study domain of North Africa. Subsequently, additional screening criteria were applied simultaneously to events that
 245

occurred within these dust sources. These criteria include (b) high wind speed, (c) wind direction over topography, (d) high increase in dust surface concentration, and (e) steep slope. Maps (b–e) are examples of filters used in the "initial" run (see in Table 1) for 1 January 2016, at 2:30 UTC.

To maximize the likelihood of capturing predominantly fresh dust emissions, high wind speed was a necessary criterion, as low wind speeds are unlikely to generate sufficient fresh dust. A single cut-off value for high wind speed was chosen as a top percentile of the 10-year average wind speed over the whole domain. Similarly, a single threshold slope was used to select the events over prominent terrain variations. Dust events occurring over relative flat surfaces were excluded to magnify the potential signals of shifted PSD due to terrain variation. Wind direction over slopes was categorized following procedures described in Section 2.1 and a cut-off angle smaller than 45° was used to exclusively select typical uphill, tangential, or downhill winds over slopes. Another criterion for increasing the probability of capturing dominantly fresh emissions was identifying sharp increases in surface concentrations. This approach favored the initiation of significant dust emissions with relative clean background dust levels. Examples of selected dust events based on each of the above criteria at 2:30 UTC on 1 January 2016, are provided in Fig. 4(b–e), using the configurations for the "initial" run (i.e., a cut-off angle of 10° for categorization of wind direction, the 80th percentile as threshold for high wind speeds and steep slope, and 80% as the threshold ratio of the increased surface dust concentration to the total dust concentration as shown in Table 1).

We performed several sensitivity tests to account for the uncertainties associated with the criteria used for event selection. We perturbed each of the threshold percentiles or the cut-off values used in the "initial" run in a pair of sensitivity runs. Specifically, we added and subtracted 10% from the threshold percentiles of 80% used for screening dust sources, steep slope, high wind speed, and high fraction of fresh emissions. Cut-off angles, β of 5° and 20° were tested compared to the initial 10° for typical wind direction. Configurations of all the sensitivity runs are shown in Table 1. A combination of all the stricter criteria was used in the "final" run.

Table 1. Thresholds or cut-off values used in all runs. Locations where the 10-year average surface dust concentration is above the threshold percentile value of all locations were designated as dust sources. Events over dust sources with slope and wind speed above the threshold percentiles of temporally averaged values over the whole domain, and increases in dust surface concentration above the threshold values were selected. The wind direction relative to topography was assigned using the cut-off angle. Values marked in bold represent the different criteria compared to the "initial" run.

Test name	Dust sources threshold percentile	Wind direction cut-off angle	Slope threshold percentile	Wind speed threshold percentile	Increase in dust surface concentration threshold
Initial	80	10°	80	80	80%
90%source	90	10°	80	80	80%
70%source	70	10°	80	80	80%
5cutoff	80	5°	80	80	80%
20cutoff	80	20°	80	80	80%
90%slope	80	10°	90	80	80%
70%slope	80	10°	70	80	80%

90%wdsp	80	10°	80	90	80%
70%wdsp	80	10°	80	70	80%
90%scconc	80	10°	80	80	90%
70%scconc	80	10°	80	80	70%
Final	90	5°	90	90	90%

274

275 **2.4 Statistical analysis**

276 Based on the selected events for “fresh” dust emissions, we explored the relationships between wind conditions and the PSD
 277 of emitted dust, taking into consideration the effects of various meteorological and landscape factors. Specifically, the
 278 dependent variable was the coarse fraction of surface dust, and the independent variables of focus were the wind speed and the
 279 slope associated with uphill, tangential, and downhill winds. The five additional independent variables are environmental
 280 variables that can potentially affect dust PSD as well as the relationships between dust PSD and wind conditions, including
 281 the continuous variables of year and soil moisture, and the categorical variables of time of day, season, and soil texture type.
 282 Dust events with missing values in soil texture class or wind direction type were excluded.

283 Exploratory data analysis was first conducted to assess data quality, identify intrinsic patterns, and guide the selection of
 284 appropriate statistical models. We selected and modified our statistical models based on their adherence to model assumptions,
 285 ability to explain the variability in the coarse fraction, and overall complexity. An initial choice was the multiple linear
 286 regression model which has the advantage of high explainability. We separated the slope by wind direction types to provide a
 287 more holistic representation of the effects of veering wind over topography. Significant coefficients for continuous variables,
 288 such as wind speed, represent the change in the coarse fraction of dust concentrations associated with a one-unit change in that
 289 corresponding independent variable. Categorical variables (e.g., time of day) are encoded as binary dummy variables, each
 290 representing a distinct category. The coefficients of these variables reflect the change in coarse fraction relative to the reference
 291 category chosen during the encoding process. Interaction terms can also be added to linear models in order to reflect the
 292 interplay between wind conditions and other factors. An interaction can be expressed as $x_m \times x_p$, where x_m is one of the four
 293 wind condition variables and x_p is one of the two additional continuous variables (i.e., year and soil moisture) or a dummy
 294 variable representing one of the three additional categorical variables (i.e., time of day, season, and soil texture). The
 295 adjustment in the coefficient for x_m due to x_p would be represented by $\beta_{mp}x_p$. A valid linear model requires linear
 296 relationships, normality of errors, constant variance (homoscedasticity), and low correlations among independent variables.
 297 Collinearity or multicollinearity among predictors can inflate standard errors and reduce the statistical significance of
 298 regression coefficients. To assess this, we calculated the Generalized Variance Inflation Factors (GVIFs) for all predictors in
 299 the linear models using the VIF function in R (R. Core Team, 2023). For categorical variables, the GVIFs were adjusted by
 300 the degrees of freedom (Df), expressed as $GVIF^{1/(2-Df)}$. An adjusted GVIF of 1 (the smallest value) indicates no collinearity,
 301 while values below 5 generally suggest low and acceptable collinearity.

302 When assumptions of normality and constant variances were violated, we attempted standardization and transformations,
303 including the Box-Cox transformation (Box and Cox, 1964) and the logit transformation (Berkson, 1944), to tackle these
304 issues. We also tested weighted linear regression, also known as weighted least squares (WLS) (Kiers, 1997), which can handle
305 non-constant variance (heteroscedasticity) by assigning weights to observations. In addition, Beta regression models were
306 implemented, which are particularly useful for fractional variables that range between 0 and 1, such as the coarse fraction in
307 this study (Douma and Weedon, 2019). Beta regression has been previously applied to air quality-related health metrics within
308 the standard unit interval (Lu et al., 2021) and to particle size data with skewed distributions (Peleg, 2019).

309 Several evaluation metrics were used to compare model performance, including the root mean square error (RMSE), the mean
310 absolute error (MAE), the adjusted coefficient of determination (adjusted R^2 , which evaluates the amount of variability in the
311 coarse fraction explained by the model while penalizing model complexity). Higher adjusted R^2 , and lower RMSE or MAE
312 values suggest that more variations of the data are captured by models. We also calculated the prediction interval accuracy at
313 the 95% confidence level, defined as the proportion of observations covered by prediction intervals. The performance metrics
314 were also averaged using the 10-fold cross-validation (CV), where the dataset was randomly divided into 10 subsets, and
315 models were trained on 9 subsets and tested on the remaining subset in each iteration, with a total of 10 iterations. All statistical
316 analyses were performed using R and the relevant packages (Zeileis and Hothorn, 2002; Grün et al., 2012; Cribari-Neto and
317 Zeileis, 2010; Fox and Weisberg, 2019; Venables and Ripley, 2002).

318 Moreover, we constructed machine learning models to account for the large dataset and potential non-linear relationships.
319 Categorical variables (wind direction, soil texture type, season, and time of day) were converted into dummy variables,
320 resulting in a total of 22 predictors when combined with continuous predictors (wind speed, slope, and year). We built Random
321 Forest and Extreme Gradient Boosting (XGBoost) models, both are widely used regressors (Bacanin et al., 2024; Brokamp et
322 al., 2017; Keller & Evans, 2019; Zhang et al., 2022). Though both models rely on decision trees, Random Forest aggregates
323 multiple trees trained on randomly sampled subset of data, whereas the XGBoost sequentially refines decision trees through
324 iterative training. Model hyperparameters were fine-tuned to maximize the predictive performance, with the search grids
325 determined based on sample size, predictor count, and computational efficiency. The search grids and the optimal
326 hyperparameter combinations are listed in Table S1. As with the linear models, we assessed the accuracy of prediction interval
327 coverage at 95% confidence level through 10-fold CV. Machine learning models are known to have high prediction accuracy
328 but can be challenging to interpret. One technique to assess the contribution of individual predictors to the coarse fraction
329 based on decision trees is the SHapley Additive exPlanations (SHAP) analysis, which was performed on the optimized models.
330 These analyses were conducted using Python packages including scikit-learn (version 1.2.2; Pedregosa et al., 2011), xgboost
331 (version 1.7.6; Chen and Guestrin, 2016), and shap (version 0.44.0; Lundberg and Lee, 2017).

332 Eventually, the more complex models did not outperform the multiple linear models to a large extent. Given their high
333 explainability, ability to incorporate interactions between predictors, and competitive performance, we ultimately selected

334 linear models for further analysis. SHAP results from the machine learning models were also included for cross-validating key
335 findings. More details on the model performance and results are described in Section 3.3.

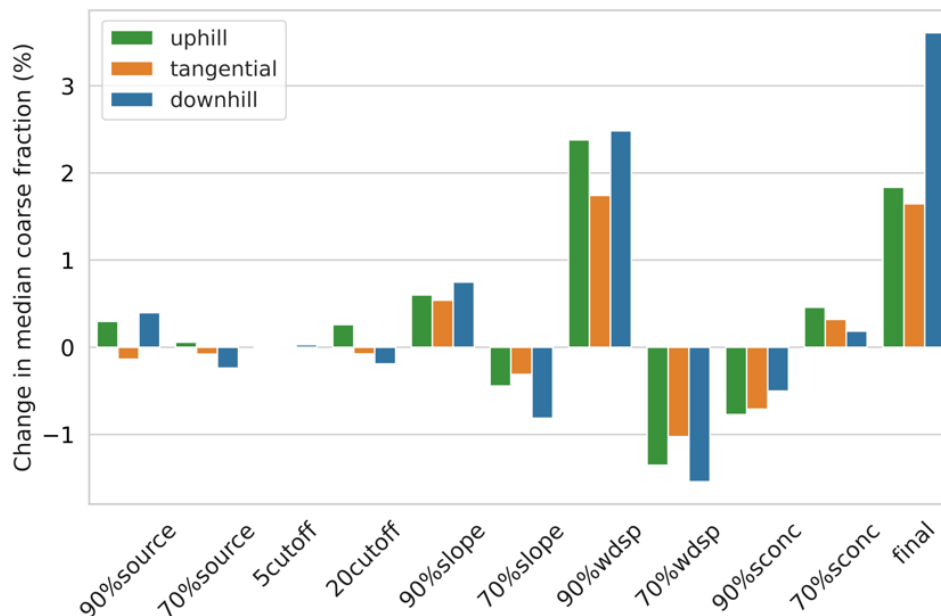
336

337 **3 Results and Discussion**

338 **3.1 Sensitivity tests show minor variations**

339 As a result of the screening processes, a total number of 461,183 dust events were identified in the “initial” run and 25,884
340 events were identified in the “final” run from around 3.5 billion records of dust concentrations at specific locations and times.
341 Figure 5 shows the percentage changes in median coarse fraction by wind direction types from all sensitivity runs. In general,
342 nearly all perturbations of any single screening criterion result in around $\pm 1\%$ of changes in average or median coarse fraction
343 grouped by wind direction. The exception is restricting wind speed to the top 10% percentile (the “90%wdsp” run), which
344 leads to a roughly 2% increase in the median values for each wind direction type. Coarse fraction of dust emissions with
345 downhill winds are usually more sensitive to the threshold values used for screening than emissions with the other two wind
346 directions. When all criteria were restricted simultaneously in the “final” run, the median coarse fraction of dust emission
347 increases by less than 2% under tangential or uphill winds and around 3.5% under downhill winds. Considering the minor
348 variations in coarse fraction among sensitivity runs, we decided to focus on one run for more detailed analysis. The “final” run
349 was chosen because, in theory, the selected events are most representative for fresh dust emissions.

350



351

352 **Figure 5.** Percentage change in the median coarse fraction by wind direction type for all sensitivity runs as compared to the “initial” run.

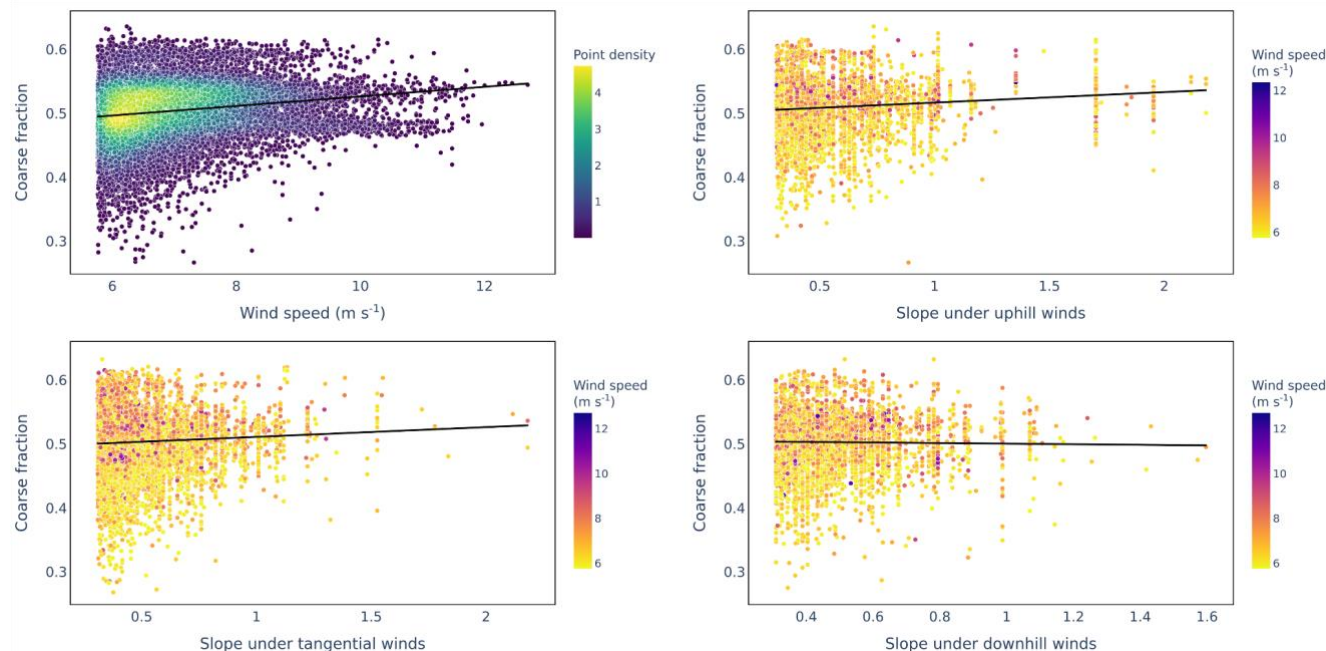
353

354 **3.2 Exploratory analysis**

355 To gain an impression of the general distribution of the data, we started with plotting the dust coarse fraction against four
356 variables of wind conditions in Fig. 6. Scatter points in the panel for wind speed are color-coded by number of overlapping
357 observations, and data points in other three panels for slopes are color-coded by wind speed. Across all four panels, a pattern
358 of heteroscedasticity is revealed, that is, the variance of coarse fraction is greater for dust events associated with lower wind
359 speed or slope than for those with high wind speed or slope. The vertically aligned scatter points with varying colors at a slope
360 of around 1.7 in the panel for “slope under uphill winds” represent 93 dust events that occurred at a same location under
361 different wind speeds near the northern border of Western Sahara during 2007–2016, illustrating how a larger number of dust
362 events can lead to higher variance. No obvious non-linear relationships between the four wind condition variables and the
363 coarse fraction are observed. The trend lines based on simple linear regression models of the coarse fraction against each wind
364 condition variable indicate general trends in the dust PSD with varying wind conditions, but the significance of these
365 relationships is not assured. Additional plots for the soil moisture and slope under three wind conditions with color-codes
366 representing the density of overlapping data points is presented in Fig. S2.

367

368



369

370 **Figure 6.** Scatter plots and linear trend lines of relationships between the coarse fraction of surface dust concentration and the wind speed
371 and the slope under three different wind directions. In the upper left panel for wind speed, the color-codes present the number of overlapping
372 data points. In the other three panels for slope, the color of each scatter point represents the associated wind speed for the dust event.

373

374 **3.3 General associations between wind conditions and dust coarse fraction**

375 The absence of obvious non-linear relationships between coarse fraction and wind conditions from the exploratory analysis
376 further motivated us to initially construct linear regression models, in addition to it being a common starting point. The linear
377 model including all independent variables but no interactions has an adjusted R^2 value of 0.224, RMSE with 10-fold CV of
378 0.070, and MAE with 10-fold CV of 0.059. Additionally, we added all possible interactions into the model and fine-tuned it
379 by removing the insignificant interaction terms. The resulting model with interactions has similar performance, with the
380 adjusted R^2 of 0.239, RMSE with 10-fold CV of 0.070, and MAE with 10-fold CV of 0.058. The somewhat weak correlations
381 may be related to factors that are not included in the model, such as deposition, variability within the same categories of soil
382 texture, etc. Residual analyses indicate violations of the assumptions of evenly distributed variance and normality (Fig. S3).
383 We attempted to address these issues and improve model performance through various linear model adaptations but only
384 obtained indefinite or marginal improvements—standardizing the coarse fraction and wind conditions variables yields an
385 adjusted R^2 of 0.241, RMSE with 10-fold CV of 1.678, and MAE with 10-fold CV of 1.420; and logit transformation on the
386 coarse fraction generates an adjusted R^2 of 0.237, RMSE with 10-fold CV of 1.420, and MAE with 10-fold CV of 0.487.
387 Furthermore, the Box-Cox transformation, weighted least squares (WLS), or Beta regression models with the best-performing
388 configuration (with a log-log link function for the mean and an identity link function for the dispersion) all failed to resolve
389 heteroscedasticity in the residuals with respect to wind condition variables. For the machine learning models, the optimized
390 Random Forest and XGBoost models achieved R^2 values of 0.407 and 0.474, respectively, which dropped to 0.259 and 0.273
391 after 10-fold CV, indicating potential overfitting. The coverage rates of prediction intervals with the 10-fold CV are 92.5% for
392 Random Forest and 54.4% for XGBoost, both lower than the 94.0% coverage by the linear models both with and without
393 interactions. Linear models outperforming machine learning models on prediction accuracy strongly encourages the selection
394 of linear models. Considering their comparative satisfactory performance, simplicity, and directly interpretable coefficients,
395 we decided to proceed with the linear regression models among all models. We first assessed the influence of individual
396 predictors based on the linear regression model without interactions, with cross comparison with results from the machine
397 learning models (Fig. S5). Subsequently, we used the linear model with interaction terms to investigate the effects of
398 interactions among predictors.

399 Linear model without interaction terms are used to infer the general effects of wind conditions on coarse dust fraction. These
400 linear models are not intended to imply strictly linear relationships between dust PSD and wind conditions, but rather to provide
401 initial guidance on the directionality of these relationships. Although individual data points present deviations, our models
402 effectively predict the overall trend, as suggested by the response vs. fitted value plots (Fig. S4), where the predicted values

align closely with observed values and cluster around the one-to-one red line. Adjusted GVIF values for the model without regression were consistently below 2 with most values close to 1 (Table S2), indicating that multicollinearity among continuous or categorical predictors does not significantly affect the regression model. The multiple linear regression model for the dust coarse fraction includes four independent variables for wind conditions (speed and three options for slope) and additional factors that may affect the PSD of dust emissions, allowing us to investigate the effects of topographic wind conditions while controlling interferences from other environmental factors. The model can be expressed as:

$$y = \beta_0 + \beta_1 x_1 + \beta_2 x_2 + \beta_3 x_3 + \beta_4 x_4 + \beta_5 x_5 + \beta_6 x_6 + \beta_7 x_7 + \beta_8 x_8 + \beta_9 x_9 + \epsilon, \quad (3)$$

where, y represents the coarse fraction of dust emissions, x_1 represents wind speed, and x_2 , x_3 , and x_4 represent slope under uphill, tangential, and downhill winds, respectively; x_5 is the categorical variable of time of day, including three levels of morning (6:00–12:00 local time), afternoon (12:00–18:00 local time), and evening (18:00–6:00 local time); x_6 is the categorical variable of season, comprising DJF (winter months of December, January, and February), MAM (spring months of March, April, and May), JJA (summer months of June, July, and August), and SON (autumn months of September, October, and November); x_7 and x_8 represent the continuous variables of year and soil moisture; and x_9 is the categorical variable of soil texture class, which contains eight levels of the FAO soil texture classes (Jahn et al., 2006). The coefficients β_i represent the expected changes in the response variable y per unit increase in the continuous predictor x_i , and the difference in y relative to the reference category for categorical predictor x_i , while holding all other variables constant. The ϵ represents the residuals of the model. The default coarse fraction is cf2 (defined in Section 2.1), and the corresponding estimated values, standard errors, and significance of the wind condition coefficients are presented in Table 2, with full details of all coefficients in Table S3. As noted in Section 2.1, we also tested two alternative definitions of coarse fraction (cf1 and cf3) and compared the estimated coefficients with their statistical significance in Table S4. The coefficient estimates based on cf2 and cf3 are largely consistent, whereas those based on cf1 show some distinct patterns. Given that dust in the top bin (12–20 μm) falls into the “super coarse” dust category ($> 10 \mu\text{m}$; Meng et al., 2022), these results suggest that super coarse dust responds differently to varying wind conditions compared to other coarse dust. Therefore, the cf2 definition serves as a robust representation of coarse dust particles.

The coefficient for wind speed from the linear model is statistically significant and positive (Table 2), suggesting that controlling the effects of other factors, the coarse fraction of dust emissions increases with the wind speed. This result is consistent with the SHAP analyses on both machine learning models as showcased in the SHAP summary plot (Fig. S5), where purple data points with high wind speed are concentrated on the right side of the vertical centerline and yellow points with lower wind speed dominate the left side, indicating a positive correlation between wind speed and coarse fraction. The observed trend contradicts implications of the theory based on the saltation-bombardment emission mechanism, which predicts

435 that higher kinetic energy of impact particles from greater wind speed can intensify the disintegration of soil aggregates and
 436 thus the release of finer particles (Shao, 2001; Alfaro et al., 1997). Conversely, our result aligns with the observed shift in the
 437 dominant emission mechanism from “shaking-off” of submicron particles to the generation of coarser microparticles from
 438 fragmentation as the velocity of saltating particles increases (Malinovskaya et al., 2021). An alternative explanation for the
 439 observed positive effect of wind speed on dust size at emission is related to soil conditions (Ishizuka et al., 2008; Panebianco
 440 et al., 2023). Emissions of super coarse dust ($> 10 \mu\text{m}$) increased with wind speed while the emissions of ultrafine dust ($< 1 \mu\text{m}$) remained nearly invariant over sandy soil (Panebianco et al., 2023); in addition, the fraction of fine dust ($< 2 \mu\text{m}$) decreased
 441 with friction velocity on slightly crusted surfaces (Ishizuka et al., 2008). These phenomena were likely due to weaker cohesive
 442 forces and thus easier emission for coarse particles than fine particles. Though our sensitivity test using cfl rejects the increased
 443 emission of super coarse dust with wind speed (Table S4), unmeasured changes in the fine dust emissions leading to an overall
 444 higher coarse fraction remain one possibility. Soil texture and soil moisture were included in the model, but subtle
 445 discrepancies across events within the same soil class or soil moisture are not eliminated. Last but not least, since the fresh
 446 dust emissions at regional scale inevitably include transported dust, yet another potential explanation is unrelated to the
 447 emission, but to the transport process—as wind speed increases, more fresh emissions are generated, which undergo less
 448 deposition and contain a higher fraction of coarse particles than the aged background dust (González-Flórez et al., 2023).
 449

450
 451 **Table 2.** Estimates, standard errors, and p-values of wind condition coefficients for the multiple linear model of dust coarse fraction. The
 452 model includes the independent variables of wind conditions (i.e., wind speed and slope under three wind direction types), time of day,
 453 season, year, soil moisture, and soil texture. The symbols of coefficients are defined in Eq. (3).

Coefficients for Variables	Estimates	Standard errors	p-values
wind speed (β_1)	0.0075	0.0002	<0.0001
slope with uphill winds (β_2)	0.0175	0.0013	<0.0001
slope with tangential winds (β_3)	0.0081	0.0015	<0.0001
slope with downhill winds (β_4)	0.0076	0.0016	<0.0001

454
 455 The coefficients for slopes under all three wind directions from the linear regression are significant and positive (Table 2),
 456 suggesting that the coarse fraction of dust emissions increases with the slope regardless of the relative wind direction. The
 457 largest coefficient for uphill winds among all three slopes indicates that it has the strongest effect on dust coarse fraction.
 458 Similarly, the SHAP analysis on the optimized Random Forest model (Fig. S5) suggests a positive relationship between slope
 459 and coarse fraction, with uphill winds further accentuate the positive effects. The XGBoost model indicates mixed effects of
 460 wind directions but the results are less reliable due to its lower prediction accuracy. Overall, the linear model and the Random
 461 Forest model agree on the positive correlation between slope, espacially under uphill winds, and dust size. The strong increase
 462 in coarse fraction with uphill slope aligns with previous findings using large eddy simulations, which was explained by the
 463 enhancement in vertical transport of dust particles being more prominent for coarser particles (Heisel et al., 2021). In contrast,
 464 the microphysics of dust emission proposed that compared to tangential winds, uphill winds against the slope resulted in more

465 detachment of fine particles from the surface of soil aggregates on the windward slope due to the secondary aeolian structures,
466 and meanwhile less ejection of coarse particles from the fragmentation of soil aggregates upon hitting the leeward slope
467 (Malinovskaya et al., 2021). Our results suggest that at the regional scale, the effect of near-source transport of emitted dust at
468 scales of hundreds to thousands of meters dominates over the impact of microphysics of dust emission related to secondary
469 dune structure at scales of centimeter to meters. The overall elevated coarse fraction with slopes might be attributed to the
470 orographic wind channelling (Rosenberg et al., 2014), increased availability of coarser particles on hills (Samuel-Rosa et al.,
471 2013; Washington et al., 2006) and their greater mobility under gravity. Effects of slope under tangential and downhill winds
472 are less pronounced, with linear model suggesting their weaker positive relationships with coarse fraction compared to uphill
473 winds (Table 2), and the Random Forest model indicating negative impacts of tangential and downhill wind directions on
474 coarse fraction even though the effect of slope is positive (Fig. S5). These weaker effects can possibly be explained by the lack
475 of effective enhancement in vertical transport of coarse particles on the windward side of slopes.

476 **3.4 Associations between wind conditions and dust coarse fraction under varying environmental conditions**

477 Interaction terms in the model allow us to investigate how the relationships between wind conditions and dust coarse fraction
478 may vary depending on the additional variables for time and surface characteristics. The model including all significant
479 interactions is shown in Eq. (4). Results for coefficients related to the interactions are shown in Table 3 and the complete
480 results are included in Table S5.

$$481 \quad y = \beta_0 + \beta_1 x_1 + \beta_2 x_2 + \beta_3 x_3 + \beta_4 x_4 + \beta_5 x_5 + \beta_6 x_6 + \beta_7 x_7 + \beta_8 x_8 + \beta_9 x_9 + \beta_{15} x_1 x_5 + \beta_{16} x_1 x_6 + \beta_{18} x_1 x_8 + \beta_{25} x_2 x_5 + \\ 482 \quad \beta_{26} x_2 x_6 + \beta_{28} x_2 x_8 + \beta_{35} x_3 x_5 + \beta_{38} x_3 x_8 + \beta_{46} x_4 x_6 + \epsilon, \quad (4)$$

484 where, $x_1 - x_9$, y , and $\beta_1 - \beta_9$ are the same as in Eq. (3). The β_{ij} are coefficients for interactions between x_i ($1 \leq i \leq 4$) and
485 x_j ($5 \leq j \leq 9$) and their interpretations are described in Section 2.4.

487 With interactions in the model, the coefficient β_1 indicates the slope of linear correlation between wind speed and the coarse
488 fraction when the variables that have interactions with wind speed are at the reference levels for categorical variables (i.e.,
489 “afternoon” for time of day and “DJF” for season) or at zero for continuous variable (i.e., soil moisture). Adjustments of the
490 correlation under other conditions are indicated by the coefficients for interactions with wind speed (β_{15} , β_{16} , and β_{18}). The
491 overall coefficient for wind speed stays positive with varying time of day and season, except for the rare cases when soil
492 moisture is high (> 50%), which agrees with the results from the model without interactions (Table 2). As suggested by the
493 adjustments of coefficients, the positive correlation between wind speed and coarse fraction is weakened during events that
494 happen in the afternoon, in summer, or are associated with higher soil moisture. All these conditions are typical for haboob
495 dust storms which are capable of generating intense dust emissions (Heinold et al., 2013; Knippertz, 2017). Therefore, a

496 potential explanation for the observed patterns is that the dust PSD dependency on wind speed is reduced during convective
 497 conditions associated with haboobs. Reasons behind the weakened correlation could be related to turbulent atmospheric
 498 conditions. Based on the above assumption that the coarse fraction increases with wind speed due to the associated higher
 499 proportion of fresh emissions, during convective events, the role of turbulent flows in keeping dust particles suspended
 500 regardless of the magnitude of wind speed may blur the effects of wind speed. Moreover, the positive relationship between
 501 wind speed and coarse fraction diminishes with soil moisture. Higher soil moisture may inhibit fresh dust emissions, which,
 502 as discussed in Section 3.3, potentially contribute to the positive correlation between wind speed and coarse dust fraction,
 503 thereby weakening the correlation.

504

505 Table 3. Estimates, standard errors, and p-values of the interaction coefficients for the multiple linear model of dust coarse
 506 fraction. The model includes the independent variables of wind conditions (i.e., wind speed and slope under three wind
 507 direction types), time of day, season, year, soil moisture, and soil texture, as well as significant interaction terms between wind
 508 conditions and other independent variables. The interaction coefficients represent wind conditions (speed and direction) under
 509 various situations of time of day, season, and soil moisture. The symbols of coefficients are defined in Eq. (3) and (4).
 510 Statistically significant (at 0.05 significance level) coefficients are bolded and their p-values are marked with “*”, among
 511 which the negative coefficients are italicized.

Multiple linear model coefficients for wind speed under various conditions			
	Estimates	Standard errors	p-values
Afternoon, DJF, and soil moisture of 0 (reference levels; β_1)	0.0076	0.0007	<0.0001*
Adjustments with time of day (β_{15})			
evening	0.0122	0.0006	<0.0001*
morning	0.0016	0.0006	0.0058*
Adjustments with season (β_{16})			
JJA	<i>-0.0028</i>	0.0007	<0.0001*
MAM	<i>-0.0023</i>	0.0006	0.0003*
SON	-0.0003	0.0007	0.6500
Adjustments with soil moisture (β_{18})	<i>-0.0154</i>	0.0029	<0.0001*
Multiple linear model coefficients for slope with uphill winds under various conditions			
	Estimates	Standard errors	p-values
Afternoon, DJF, and soil moisture of 0 (reference levels; β_2)	0.0135	0.0030	<0.0001*
Adjustments with time of day (β_{25})			
evening	0.0061	0.0024	0.0118*
morning	0.0159	0.0026	<0.0001*
Adjustments with season (β_{26})			
JJA	<i>-0.0098</i>	0.0028	0.0005*
MAM	<i>-0.0138</i>	0.0029	<0.0001*
SON	-0.0056	0.0031	0.0672
Adjustments with soil moisture (β_{28})	0.0521	0.0107	<0.0001
Multiple linear model coefficients for slope with tangential winds under various conditions			
	Estimates	Standard errors	p-values
Afternoon, soil moisture of 0	-0.0038	0.0025	0.1261

(reference levels; β_3)			
Adjustments with time of day (β_{35})			
evening	0.0134	0.0024	<0.0001*
morning	0.0110	0.0027	<0.0001*
Adjustments with soil moisture (β_{38})	0.0351	0.0115	0.0022*
Multiple linear model coefficients for slope with downhill winds under various conditions			
	Estimates	Standard errors	p-values
DJF (reference level; β_4)	0.0148	0.0026	<0.0001*
Adjustments with season (β_{46})			
JJA	-0.0101	0.0031	0.0011*
MAM	-0.0105	0.0032	0.0011*
SON	-0.0090	0.0036	0.0116*

512

513 The adjustments of the relationship between slope and coarse fraction with other environmental variables are generally
 514 consistent across three wind direction types. Overall, the coefficients for slope with three wind directions stay positive under
 515 most circumstances, aligning with results from the model without interactions (Table 2). Notably, the effect of the uphill slope
 516 is strongest in the morning. Unlike Harmattan surges, which can induce dust emission throughout the day, or haboob storms,
 517 which mostly occur in the afternoons, dust uplift due to the breakdown of night-time low-level jets (NLLJs) is limited to the
 518 period around sunrise to midday (Fiedler et al., 2015; Heinold et al., 2013). Therefore, the result indicates that the role of uphill
 519 slope in facilitating transport of coarse dust is particularly relevant during emissions related to NLLJs. Moreover, the effect of
 520 slope in increasing coarse fraction is weakest during afternoon events under both uphill and tangential winds. With both uphill
 521 and downhill winds, the positive correlation between slope and coarse fraction is the strongest in winter, and the weakest in
 522 spring and summer. The reduced correlation of dust PSD with uphill slope in both afternoon and summer suggests a diminished
 523 effect of slope during haboob dust storms. This can be explained by the stronger turbulence associated with convective storms,
 524 which readily stirs up the air and facilitate particle transport, thereby weakening the additional effect of uphill slope by
 525 elevating coarse particles through flow separation.

526 The effect of slope on increasing coarse fraction of dust also becomes more apparent with increasing soil moisture under uphill
 527 and tangential winds. Low soil moisture might be associated with low water vapor content in lower-Saharan Air Layer, which
 528 can lead to continued vertical motions of the atmosphere into the night due to increased atmospheric longwave heating (Ryder,
 529 2021). Conversely, the air is more stable with higher relative humidity, making the enhancement by topography more critical
 530 for the transport of coarse dust.

531

532 **4 Conclusion**

533 This study aims to explore the relationship between topographic wind conditions and particle size distribution (PSD) of dust
534 emissions on a regional scale through data analysis. The Multiscale Online Nonhydrostatic Atmosph^{er}e Chemistry model
535 (MONARCH) dust concentrations were first evaluated against flight measurements of fresh dust emissions from the 2011
536 Fennec campaign and were proven to be effective in capturing concentrations of coarse to super coarse dusts in fresh dust
537 emissions. For our analysis, size-resolved surface dust mass concentrations from the MONARCH dust reanalysis over the
538 Sahara during 2007–2016 were condensed into an index of coarse fraction (the ratio of the sum of concentrations in the top
539 two bins (6–20 μm) to the total concentration in eight bins (0.2–20 μm)), serving as the proxy for size distribution. Information
540 on wind vectors and soil moisture, elevation, and soil texture was obtained from the Modern-Era Retrospective analysis for
541 Research and Applications (MERRA-2) reanalysis data, the NASA Shuttle Radar Topography Mission Global 3 arc-second
542 (SRTM GL3) dataset, and the inputs to the Global Land Data Assimilation System version 2 (GLDAS2) Noah land surface
543 model, respectively. Several highly selective criteria were applied to maximize the probability of selecting fresh dust emissions
544 with typical wind conditions over topography. Scatter plots of coarse fraction against four wind conditions variables (i.e., wind
545 speed, slope under uphill, tangential, and downhill winds) reveal unevenly distributed variance without obvious non-linear
546 trends. We ultimately selected the multiple linear models after testing several model variations to quantify and explain the
547 trends in data, with key findings cross-validated using machine learning models.

548 The linear model without and with significant interaction terms can explain 22% and 24% of the variability of coarse fraction,
549 respectively. The model, however, fails to fulfil the assumptions on homoscedasticity (constant variance) and normality, and
550 this issue could not be resolved by other parametric modelling approaches including linear regression models with
551 transformations of variables, weighted least square, or Beta regression models with several options for link functions. The
552 strong intrinsic pattern of non-constant variance and the abundance of data points require more advanced models, which is
553 beyond the scope of our current work. Other uncertainties arose from the varying original resolution of datasets and the
554 resampling process. Moreover, even though we applied multiple criteria to exclusively pick fresh dust emissions, we cannot
555 totally exclude the portion of transported dust. The analysis focuses on the general trend for North Africa, and more detailed
556 insights rely on analysis for smaller geographic domains.

557 Despite some limitations, the multiple linear models achieved high predictive accuracy—over 94% under 10-fold cross-
558 validation (CV)—demonstrating their capability to provide meaningful insights for interpretation. The optimized Random
559 Forest model, which attained 92% predictive accuracy with 10-fold CV despite potential overfitting, adding insights to the
560 influence of each predictor by applying the SHapley Additive exPlanations (SHAP) analysis. Both the linear and machine
561 learning models consistently reveal positive associations between coarse dust fraction and both wind speed and slope. The
562 impact of wind speed may possibly be attributed to a higher proportion of fresh emissions, or a greater resistance of surface
563 soil to disintegration into fine dust particles. The persistent influence of slope on increasing coarse fraction might be related to
564 meteorological (e.g., the orographic wind channelling) and soil conditions (e.g., increased availability and gravitational

565 mobility of coarser particles on hills). The effect of slope is most pronounced under uphill winds, highlighting the transport
566 enhancement by topography over distances of hundreds to thousands of meters, which overrides the potential impact of local
567 emission mechanisms at scales of centimeters to meters. Including interaction terms in the model allows us to investigate shifts
568 in the effects of wind conditions on dust size under different environmental conditions. The positive correlation between wind
569 speed and coarse fraction diminishes during afternoon and summer events and under high soil moisture. This reduction is
570 likely due to decreased differences in dust size distribution by deposition during haboob convective storms when turbulence
571 is strong. The uphill slope exhibits the strongest effect on increasing dust size in the morning, suggesting that the enhanced
572 vertical transport is particularly effective in uplifting coarse dust during emissions related to the breakdown of night-time low-
573 level jets. The effect of uphill slope is weakened during summer and afternoons, indicating that turbulence during haboob dust
574 storms has competing effects in sustaining airborne coarse dust.

575 This work provides insights into the controlling factors of dust PSD on a regional scale using a meta-analysis of a 10-year dust
576 reanalysis dataset, which complements the accumulating knowledge from recent field measurements. The study highlights the
577 overlapping effects and interactions among various environmental factors on size distribution of dust emissions and calls for
578 more work focusing on different factors and their interactions at various scales. Meanwhile, the workflow for screening fresh
579 dust events developed in this study will facilitate future work of utilizing datasets at different scales.

580

581 **Data Availability**

582 The open-access MONARCH dust reanalysis data, prepared by the Barcelona Supercomputing Center (BSC), are available at
583 https://earth.bsc.es/thredds_dustclim/homepage/. The Modern-Era Retrospective analysis for Research and Applications
584 (MERRA-2) data (Gelaro et al., 2017) are managed by the NASA Goddard Earth Sciences (GES) Data and Information
585 Services Center (DISC) and can be accessed at <https://disc.gsfc.nasa.gov/datasets?project=MERRA-2>. The NASA Shuttle
586 Radar Topography Mission Global 3 arc-second (SRTM GL3) dataset is available at
587 <https://lpdaac.usgs.gov/products/srtmgl3v003/>. The soil texture map input to the Global Land Data Assimilation System
588 version 2 (GLDAS2) Noah land surface model (Rodell et al., 2004) is described and provided by NASA at
589 <https://ldas.gsfc.nasa.gov/gldas/soils>.

590

591 **Competing Interests**

592 The authors declare that they have no conflict of interests.

593

594 **Author Contribution**

595 HF secured funding for the research. HF and XH conceptualized the study, developed methodology for data collection and
596 processing, and provided the scientific interpretation of the results. XH processed the data and created the data visualizations.
597 WG conducted the statistical analysis of the processed data, drafted the corresponding methods (Section 2.4), and verified the
598 initial interpretation based on the statistical results. XH wrote the initial draft of the manuscript, and all authors contributed to
599 the final version.

600

601 **Acknowledgements**

602 This work was supported by the National Aeronautics and Space Administration (NASA) under Grant 80NSSC20K1532. We
603 are grateful to Dr. Clair Ryder for her guidance on the Fennec campaign data, and to Dr. Carlos Pérez García-Pando for
604 reviewing the manuscript and providing valuable insights into the interpretation of the results.

605

606 **References**

607 Adebiyi, A. A. and Kok, J. F.: Climate models miss most of the coarse dust in the atmosphere, *Science Advances*, 6,
608 doi:10.1126/sciadv.aaz9507, 2020.

609 Alfaro, S. C., Bouet, C., Khalfallah, B., Shao, Y., Ishizuka, M., Labiad, M., Marticorena, B., Laurent, B., and Rajot,
610 J. L.: Unraveling the Roles of Saltation Bombardment and Atmospheric Instability on Magnitude and Size
611 Distribution of Dust Emission Fluxes: Lessons From the JADE and WIND-O-V Experiments, *Journal of*
612 *Geophysical Research: Atmospheres*, 127, doi:10.1029/2021jd035983, 2022.

613 Bacanin, N., Perisic, M., Jovanovic, G., Damaševičius, R., Stanisic, S., Simic, V., Zivkovic, M., and Stojic, A.: The
614 explainable potential of coupling hybridized metaheuristics, XGBoost, and SHAP in revealing toluene behavior
615 in the atmosphere, *Science of The Total Environment*, 929, 172195, doi:10.1016/j.scitotenv.2024.172195, 2024.

616 Berkson, J.: Application of the Logistic Function to Bio-Assay, *Journal of the American Statistical Association*, 39,
617 357–365, doi:10.2307/2280041, 1944.

618 Box, G. E. P. and Cox, D. R.: An Analysis of Transformations, *Journal of the Royal Statistical Society Series B:*
619 *Statistical Methodology*, 26, 211–243, doi:10.1111/j.2517-6161.1964.tb00553.x, 1964.

620 Brasseur, G. P. and Jacob, D. J.: Modeling of Atmospheric Chemistry, Cambridge University Press, Cambridge,
621 doi:10.1017/9781316544754, 2017.

622 Brokamp, C., Jandarov, R., Rao, M. B., LeMasters, G., and Ryan, P.: Exposure assessment models for elemental
623 components of particulate matter in an urban environment: A comparison of regression and random forest
624 approaches, *Atmospheric Environment*, 151, 1–11, doi:10.1016/j.atmosenv.2016.11.066, 2017.

625 Caton Harrison, T., Washington, R., Engelstaedter, S., Jones, R. G., and Savage, N. H.: Influence of Orography Upon
626 Summertime Low-Level Jet Dust Emission in the Central and Western Sahara, *Journal of Geophysical Research: Atmospheres*, 126, doi:10.1029/2021jd035025, 2021.

628 Chen, T. and Guestrin, C.: XGBoost: A Scalable Tree Boosting System, *Proceedings of the 22nd ACM SIGKDD*
629 International Conference on Knowledge Discovery and Data Mining, San Francisco, California, USA,
630 doi:10.1145/2939672.2939785, 2016.

631 Chkhetiani, O. G., Vazaeva, N. V., Chernokulsky, A. V., Shukurov, K. A., Gubanova, D. P., Artamonova, M. S.,
632 Maksimenkov, L. O., Kozlov, F. A., and Kuderina, T. M.: Analysis of Mineral Aerosol in the Surface Layer
633 over the Caspian Lowland Desert by the Data of 12 Summer Field Campaigns in 2002–2020, *Atmosphere*, 12,
634 doi:10.3390/atmos12080985, 2021.

635 Cribari-Neto, F. and Zeileis, A.: Beta Regression in R, *Journal of Statistical Software*, 34, 1–24,
636 doi:10.18637/jss.v034.i02, 2010.

637 Dee, D. P., Uppala, S., Simmons, A. J., Berrisford, P., Poli, P., Kobayashi, S., Andrae, U., Balmaseda, M., Balsamo,
638 G., and Bauer, d. P.: The ERA-Interim reanalysis: Configuration and performance of the data assimilation
639 system, *Quarterly Journal of the royal meteorological society*, 137, 553–597, 2011.

640 Di Tomaso, E., Escribano, J., Basart, S., Ginoux, P., Macchia, F., Barnaba, F., Benincasa, F., Bretonnière, P. A., Buñuel,
641 A., Castrillo, M., Cuevas, E., Formenti, P., Gonçalves, M., Jorba, O., Klose, M., Mona, L., Montané Pinto, G.,
642 Mytilinaios, M., Obiso, V., Olid, M., Schutgens, N., Votsis, A., Werner, E., and Pérez García-Pando, C.: The
643 MONARCH high-resolution reanalysis of desert dust aerosol over Northern Africa, the Middle East and Europe
644 (2007–2016), *Earth Syst. Sci. Data*, 14, 2785–2816, doi:10.5194/essd-14-2785-2022, 2022.

645 Douma, J. C. and Weedon, J. T.: Analysing continuous proportions in ecology and evolution: A practical introduction
646 to beta and Dirichlet regression, *Methods in Ecology and Evolution*, 10, 1412–1430, doi:10.1111/2041-
647 210x.13234, 2019.

648 Duce, R. A. and Tindale, N. W.: Atmospheric transport of iron and its deposition in the ocean, *Limnology and*
649 *Oceanography*, 36, 1715–1726, doi:10.4319/lo.1991.36.8.1715, 1991.

650 Dupont, S.: On the Influence of Thermal Stratification on Emitted Dust Flux, *Journal of Geophysical Research: Atmospheres*, 127, doi:10.1029/2022jd037364, 2022.

651

652 Dupont, S., Alfaro, S. C., Bergametti, G., and Marticorena, B.: Near-surface dust flux enrichment in small particles
653 during erosion events, *Geophysical Research Letters*, 42, 1992–2000, doi:10.1002/2015gl063116, 2015.

654 Farr, T. G., Rosen, P. A., Caro, E., Crippen, R., Duren, R., Hensley, S., Kobrick, M., Paller, M., Rodriguez, E., Roth,
655 L., Seal, D., Shaffer, S., Shimada, J., Umland, J., Werner, M., Oskin, M., Burbank, D., and Alsdorf, D.: The
656 Shuttle Radar Topography Mission, *Reviews of Geophysics*, 45, doi:10.1029/2005rg000183, 2007.

657 Fernandes, R., Dupont, S., and Lamaud, E.: Experimental evidence of dust flux size distribution variation along two
658 consecutive erosion seasons, *Aeolian Research*, 61, doi:10.1016/j.aeolia.2023.100863, 2023.

659 Fiedler, S., Kaplan, M. L., and Knippertz, P.: The importance of Harmattan surges for the emission of North African
660 dust aerosol, *Geophysical Research Letters*, 42, 9495–9504, doi:10.1002/2015gl065925, 2015.

661 Formenti, P., Schütz, L., Balkanski, Y., Desboeufs, K., Ebert, M., Kandler, K., Petzold, A., Scheuvens, D., Weinbruch,
662 S., and Zhang, D.: Recent progress in understanding physical and chemical properties of African and Asian
663 mineral dust, *Atmospheric Chemistry and Physics*, 11, 8231–8256, doi:10.5194/acp-11-8231-2011, 2011.

664 Fox, J. and Weisberg, S.: *An R Companion to Applied Regression*, 2019.

665 Fujiwara, M., Martineau, P., Wright, J. S., Abalos, M., Šácha, P., Kawatani, Y., Davis, S. M., Birner, T., and Monge-
666 Sanz, B. M.: Climatology of the terms and variables of transformed Eulerian-mean (TEM) equations from
667 multiple reanalyses: MERRA-2, JRA-55, ERA-Interim, and CFSR, *Atmos. Chem. Phys.*, 24, 7873–7898,
668 doi:10.5194/acp-24-7873-2024, 2024.

669 Gelaro, R., McCarty, W., Suárez, M. J., Todling, R., Molod, A., Takacs, L., Randles, C. A., Darmenov, A., Bosilovich,
670 M. G., Reichle, R., Wargan, K., Coy, L., Cullather, R., Draper, C., Akella, S., Buchard, V., Conaty, A., da Silva,
671 A. M., Gu, W., Kim, G.-K., Koster, R., Lucchesi, R., Merkova, D., Nielsen, J. E., Partyka, G., Pawson, S.,
672 Putman, W., Rienecker, M., Schubert, S. D., Sienkiewicz, M., and Zhao, B.: The Modern-Era Retrospective
673 Analysis for Research and Applications, Version 2 (MERRA-2), *Journal of Climate*, 30, 5419–5454,
674 doi:10.1175/JCLI-D-16-0758.1, 2017.

675 Gesch, D., Williams, J., and Miller, W.: A comparison of US geological survey seamless elevation models with shuttle
676 radar topography mission data, *IGARSS 2001. Scanning the Present and Resolving the Future. Proceedings.*
677 IEEE 2001 International Geoscience and Remote Sensing Symposium (Cat. No. 01CH37217), 754–756, 2001.

678 Ginoux, P., Chin, M., Tegen, I., Prospero, J. M., Holben, B., Dubovik, O., and Lin, S.-J.: Sources and distributions of
679 dust aerosols simulated with the GOCART model, *Journal of Geophysical Research: Atmospheres*, 106, 20255
680 –20273, doi:10.1029/2000JD000053, 2001.

681 Ginoux, P., Prospero, J. M., Gill, T. E., Hsu, N. C., and Zhao, M: Global-scale attribution of anthropogenic and natural
682 dust sources and their emission rates based on MODIS Deep Blue aerosol products, *Rev. Geophys.*, 50, RG3005,
683 doi:10.1029/2012RG000388, 2012.

684 González-Flórez, C., Klose, M., Alastuey, A., Dupont, S., Escribano, J., Etyemezian, V., Gonzalez-Romero, A., Huang,
685 Y., Kandler, K., Nikolic, G., Panta, A., Querol, X., Reche, C., Yus-Díez, J., and Pérez García-Pando, C.: Insights into the size-resolved dust emission from field measurements in the Moroccan Sahara, *Atmos. Chem.
686 Phys.*, 23, 7177–7212, doi:10.5194/acp-23-7177-2023, 2023.

688 Graesser, J.: GeoWombat: Utilities for geospatial data [code], <https://github.com/jgrss/geombat>, 2023.

689 Grün, B., Kosmidis, I., and Zeileis, A.: Extended Beta Regression in R: Shaken, Stirred, Mixed, and Partitioned, *Journal
690 of Statistical Software*, 48, 1–25, doi:10.18637/jss.v048.i11, 2012.

691 Heinold, B., Knippertz, P., Marsham, J. H., Fiedler, S., Dixon, N. S., Schepanski, K., Laurent, B., and Tegen, I.: The
692 role of deep convection and nocturnal low-level jets for dust emission in summertime West Africa: Estimates
693 from convection-permitting simulations, *J Geophys Res Atmos*, 118, 4385–4400, doi:10.1002/jgrd.50402, 2013.

694 Heisel, M., Chen, B., Kok, J. F., and Chamecki, M.: Gentle Topography Increases Vertical Transport of Coarse Dust
695 by Orders of Magnitude, *Journal of Geophysical Research: Atmospheres*, 126, doi:10.1029/2021JD034564,
696 2021.

697 Ishizuka, M., Mikami, M., Leys, J., Yamada, Y., Heidenreich, S., Shao, Y., and McTainsh, G. H.: Effects of soil
698 moisture and dried raindrop crust on saltation and dust emission, *Journal of Geophysical Research: Atmospheres*, 113, doi:10.1029/2008jd009955, 2008.

700 Jahn, R., Blume, H. P., Asio, V., Spaargaren, O., and Schád, P.: FAO Guidelines for Soil Description, 2006.

701 Katra, I.: Soil Erosion by Wind and Dust Emission in Semi-Arid Soils Due to Agricultural Activities, *Agronomy*, 10,
702 doi:10.3390/agronomy10010089, 2020.

703 Keller, C. A. and Evans, M. J.: Application of random forest regression to the calculation of gas-phase chemistry within
704 the GEOS-Chem chemistry model v10, *Geosci. Model Dev.*, 12, 1209–1225, 10.5194/gmd-12-1209-2019,
705 2019.

706 Kellogg, C. A. and Griffin, D. W.: Aerobiology and the global transport of desert dust, *Trends Ecol Evol*, 21, 638–644,
707 doi:10.1016/j.tree.2006.07.004, 2006.

708 Khalfallah, B., Bouet, C., Labiad, M. T., Alfaro, S. C., Bergametti, G., Marticorena, B., Lafon, S., Chevaillier, S.,
709 Féron, A., Hease, P., Henry des Tureaux, T., Sekrafi, S., Zapf, P., and Rajot, J. L.: Influence of Atmospheric
710 Stability on the Size Distribution of the Vertical Dust Flux Measured in Eroding Conditions Over a Flat Bare
711 Sandy Field, *Journal of Geophysical Research: Atmospheres*, 125, doi:10.1029/2019jd031185, 2020.

712 Kiers, H. A. L.: Weighted least squares fitting using ordinary least squares algorithms, *Psychometrika*, 62, 251–266,
713 1997.

714 Klose, M., Jorba, O., Gonçalves Ageitos, M., Escribano, J., Dawson, M. L., Obiso, V., Di Tomaso, E., Basart, S.,
715 Montané Pinto, G., Macchia, F., Ginoux, P., Guerschman, J., Prigent, C., Huang, Y., Kok, J. F., Miller, R. L.,
716 and Pérez García-Pando, C.: Mineral dust cycle in the Multiscale Online Nonhydrostatic AtmospheRe
717 CHemistry model (MONARCH) Version 2.0, *Geosci. Model Dev.*, 14, 6403–6444, doi:10.5194/gmd-14-6403-
718 2021, 2021.

719 Knippertz, P.: Mineral Dust Generation across Northern Africa and Its Impacts, in: *Oxford Research Encyclopedia of*
720 *Climate Science*, doi:10.1093/acrefore/9780190228620.013.516, 2017.

721 Knippertz, P., Deutscher, C., Kandler, K., Müller, T., Schulz, O., and Schütz, L.: Dust mobilization due to density
722 currents in the Atlas region: Observations from the Saharan Mineral Dust Experiment 2006 field campaign,
723 *Journal of Geophysical Research: Atmospheres*, 112, doi:10.1029/2007jd008774, 2007.

724 Kok, J. F.: Does the size distribution of mineral dust aerosols depend on the wind speed at emission?, *Atmospheric*
725 *Chemistry and Physics*, 11, 10149–10156, doi:10.5194/acp-11-10149-2011, 2011.

726 Kok, J. F., Parteli, E. J. R., Michaels, T. I., and Karam, D. B.: The physics of wind-blown sand and dust, *Reports on*
727 *Progress in Physics*, 75, 106901, doi:10.1088/0034-4885/75/10/106901, 2012.

728 Kok, J. F., Albani, S., Mahowald, N. M., and Ward, D. S.: An improved dust emission model – Part 2: Evaluation in
729 the Community Earth System Model, with implications for the use of dust source functions, *Atmos. Chem.*
730 *Phys.*, 14, 13043 –13061, doi:10.5194/acp-14-13043-2014, 2014.

731 Kok, J. F., Storelvmo, T., Karydis, V. A., Adebiyi, A. A., Mahowald, N. M., Evan, A. T., He, C., and Leung, D. M.:
732 Mineral dust aerosol impacts on global climate and climate change, *Nature Reviews Earth & Environment*, 4,
733 71–86, doi:10.1038/s43017-022-00379-5, 2023.

734 Lu, S., Symonds, P., Verschoor, N., Chalabi, Z., Taylor, J., and Davies, M.: Use of Beta Regression to investigate the
735 link between home air infiltration rate and self-reported health, *Journal of Physics: Conference Series*, 2069,
736 doi:10.1088/1742-6596/2069/1/012178, 2021.

737 Lundberg, S. M. and Lee, S.-I.: A unified approach to interpreting model predictions, Proceedings of the 31st
738 International Conference on Neural Information Processing Systems, Long Beach, California, USA, 2017.

739 Ma, X., Gao, Q., Jiang, X., Chen, S., Gan, Y., Zhang, T., Lu, X., and Wang, X.: Direct Effects of Air Humidity on Dust
740 Aerosol Production: Evidences for the Surprising Role of Electrostatic Forces, *Geophysical Research Letters*,
741 50, doi:10.1029/2023gl103639, 2023.

742 Mahowald, N., Albani, S., Kok, J. F., Engelstaeder, S., Scanza, R., Ward, D. S., and Flanner, M. G.: The size distribution
743 of desert dust aerosols and its impact on the Earth system, *Aeolian Research*, 15, 53–71,
744 doi:10.1016/j.aeolia.2013.09.002, 2014.

745 Malinovskaya, E. A., Chkhetiani, O. G., and Maksimenkov, L. O.: Influence of Wind Direction on the Size Distribution
746 of Aeolian Microparticles, *Izvestiya, Atmospheric and Oceanic Physics*, 57, 472–485,
747 doi:10.1134/S0001433821050108, 2021.

748 Marticorena, B. and Bergametti, G.: Modeling the atmospheric dust cycle: 1. Design of a soil-derived dust emission
749 scheme, *Journal of geophysical research: atmospheres*, 100, 16415 –16430, 1995.

750 Meng, J., Huang, Y., Leung, D. M., Li, L., Adebiyi, A. A., Ryder, C. L., Mahowald, N. M., and Kok, J. F.: Improved
751 Parameterization for the Size Distribution of Emitted Dust Aerosols Reduces Model Underestimation of Super
752 Coarse Dust, *Geophys Res Lett*, 49, doi:10.1029/2021GL097287, 2022.

753

754 Mytilinaios, M., Basart, S., Ciamprone, S., Cuesta, J., Dema, C., Di Tomaso, E., Formenti, P., Gkikas, A., Jorba, O.,
755 Kahn, R., Pérez García-Pando, C., Trippetta, S., and Mona, L.: Comparison of dust optical depth from multi-
756 sensor products and MONARCH (Multiscale Online Non-hydrostatic AtmospheRe CHemistry) dust reanalysis
757 over North Africa, the Middle East, and Europe, *Atmos. Chem. Phys.*, 23, 5487–5516, doi:10.5194/acp-23-
758 5487-2023, 2023.

759 Panebianco, J. E., Avecilla, F., Funk, R., and Buschiazzo, D. E.: Influence of friction velocity and saltation intensity
760 on the particle-size distribution of dust (PM32) emitted from an agricultural soil, *Earth Surface Processes and*
761 *Landforms*, 48, 1176–1187, doi:10.1002/esp.5541, 2023.

762 Pedregosa, F., Varoquaux, G., Gramfort, A., Michel, V., Thirion, B., Grisel, O., Blondel, M., Prettenhofer, P., Weiss,
763 R., Dubourg, V., Vanderplas, J., Passos, A., Cournapeau, D., Brucher, M., Perrot, M., and Duchesnay, É.: Scikit-
764 learn: Machine Learning in Python, *J. Mach. Learn. Res.*, 12, 2825–2830, 2011.

765 Peleg, M.: Beta distributions for particle size having a finite range and predetermined mode, mean or median, *Powder*
766 *Technology*, 356, 790–794, doi:10.1016/j.powtec.2019.09.015, 2019.

767 Polymenakou, P. N., Mandalakis, M., Stephanou, E. G., and Tselepides, A.: Particle size distribution of airborne
768 microorganisms and pathogens during an Intense African dust event in the eastern Mediterranean, *Environ*
769 *Health Perspect*, 116, 292–296, doi:10.1289/ehp.10684, 2008.

770 Prospero, J. M., Blades, E., Mathison, G., and Naidu, R.: Interhemispheric transport of viable fungi and bacteria from
771 Africa to the Caribbean with soil dust, *Aerobiologia*, 21, 1–19, doi:10.1007/s10453-004-5872-7, 2005.

772 Pu, B., and Ginoux, P.: The impact of the Pacific Decadal Oscillation on springtime dust activity in Syria, *Atmos.*
773 *Chem. Phys.*, 16, 13431–13448, doi:10.5194/acp-16-13431-2016, 2016.

774 R. Core Team: R: A Language and Environment for Statistical Computing, 2023.

775 Reynolds, C. A., Jackson, T. J., and Rawls, W. J.: Estimating soil water-holding capacities by linking the Food and
776 Agriculture Organization Soil map of the world with global pedon databases and continuous pedotransfer
777 functions, *Water Resources Research*, 36, 3653–3662, doi:10.1029/2000wr900130, 2000.

778 Rienercker, M. M., Suarez, M., Todling, R., Bacmeister, J., Takacs, L., Liu, H.-C., Gu, W., Sienkiewicz, M., Koster, R.,
779 and Gelaro, R.: The GEOS-5 Data Assimilation System—Documentation of Versions 5.0. 1, 5.1. 0, and 5.2. 0,
780 2008.

781 Rodell, M., Houser, P. R., Jambor, U., Gottschalck, J., Mitchell, K., Meng, C. J., Arsenault, K., Cosgrove, B.,
782 Radakovich, J., Bosilovich, M., Entin*, J. K., Walker, J. P., Lohmann, D., and Toll, D.: The Global Land Data
783 Assimilation System, *Bulletin of the American Meteorological Society*, 85, 381–394, doi:10.1175/BAMS-85-
784 3-381, 2004.

785 Rosenberg, P. D., Parker, D. J., Ryder, C. L., Marsham, J. H., Garcia-Carreras, L., Dorsey, J. R., Brooks, I. M., Dean,
786 A. R., Crosier, J., McQuaid, J. B., and Washington, R.: Quantifying particle size and turbulent scale dependence
787 of dust flux in the Sahara using aircraft measurements, *Journal of Geophysical Research: Atmospheres*, 119,
788 7577–7598, doi:10.1002/2013jd021255, 2014.

789 Ryder, C. L.: Radiative Effects of Increased Water Vapor in the Upper Saharan Air Layer Associated With Enhanced
790 Dustiness, *Journal of Geophysical Research: Atmospheres*, 126, doi:10.1029/2021jd034696, 2021.

791 Ryder, C. L., Highwood, E. J., Walser, A., Seibert, P., Philipp, A., and Weinzierl, B.: Coarse and giant particles are
792 ubiquitous in Saharan dust export regions and are radiatively significant over the Sahara, *Atmospheric*
793 *Chemistry and Physics*, 19, 15353–15376, doi:10.5194/acp-19-15353-2019, 2019.

794 Ryder, C. L., Highwood, E. J., Rosenberg, P. D., Trembath, J., Brooke, J. K., Bart, M., Dean, A., Crosier, J., Dorsey,
795 J., Brindley, H., Banks, J., Marsham, J. H., McQuaid, J. B., Sodemann, H., and Washington, R.: Optical

796 properties of Saharan dust aerosol and contribution from the coarse mode as measured during the Fennec 2011
797 aircraft campaign, *Atmospheric Chemistry and Physics*, 13, 303–325, doi:10.5194/acp-13-303-2013, 2013.

798 Ryder, C. L., McQuaid, J. B., Flamant, C., Rosenberg, P. D., Washington, R., Brindley, H. E., Highwood, E. J.,
799 Marsham, J. H., Parker, D. J., Todd, M. C., Banks, J. R., Brooke, J. K., Engelstaedter, S., Estelles, V., Formenti,
800 P., Garcia-Carreras, L., Kocha, C., Marenco, F., Sodemann, H., Allen, C. J. T., Bourdon, A., Bart, M., Cavazos-
801 Guerra, C., Chevaillier, S., Crosier, J., Darbyshire, E., Dean, A. R., Dorsey, J. R., Kent, J., O'Sullivan, D.,
802 Schepanski, K., Szpek, K., Trembath, J., and Woolley, A.: Advances in understanding mineral dust and
803 boundary layer processes over the Sahara from Fennec aircraft observations, *Atmospheric Chemistry and*
804 *Physics*, 15, 8479–8520, doi:10.5194/acp-15-8479-2015, 2015.

805 Samuel-Rosa, A., Dalmolin, R. S. D., and Miguel, P.: Building predictive models of soil particle-size distribution,
806 *Revista Brasileira de Ciência do Solo*, 37, 422–430, doi:10.1590/s0100-06832013000200013, 2013.

807 Santos, J., Sakagami, Y., Haas, R., Passos, J., Machuca, M., Radünz, W., Dias, E., and Lima, M.: Wind speed evaluation
808 of MERRA-2, ERA-interim and ERA-5 reanalysis data at a wind farm located in brazil, *Proceedings of the ISES*
809 *Solar World Congress*, 1 –10, 2019.

810 Shao, Y.: A model for mineral dust emission, *Journal of Geophysical Research: Atmospheres*, 106, 20239–20254,
811 doi:10.1029/2001jd900171, 2001.

812 Shao, Y., Zhang, J., Ishizuka, M., Mikami, M., Leys, J., and Huang, N.: Dependency of particle size distribution at dust
813 emission on friction velocity and atmospheric boundary-layer stability, *Atmospheric Chemistry and Physics*,
814 20, 12939–12953, doi:10.5194/acp-20-12939-2020, 2020.

815 Tanaka, T. Y. and Chiba, M.: A numerical study of the contributions of dust source regions to the global dust budget,
816 *Global and Planetary Change*, 52, 88–104, doi:10.1016/j.gloplacha.2006.02.002, 2006.

817 Venables, W. N. and Ripley, B. D.: *Modern Applied Statistics with S*, 2002.

818 Wang, R., Li, Q., Wang, R., Chang, C., Guo, Z., Li, J., and Zhou, N.: Influence of Wind Velocity and Soil Size
819 Distribution on Emitted Dust Size Distribution: A Wind Tunnel Study, *Journal of Geophysical Research:*
820 *Atmospheres*, 126, doi:10.1029/2020jd033768, 2021.

821 Wang, X., Wang, Q., Prass, M., Pöhlker, C., Moran-Zuloaga, D., Artaxo, P., Gu, J., Yang, N., Yang, X., Tao, J., Hong,
822 J., Ma, N., Cheng, Y., Su, H., and Andreae, M. O.: The export of African mineral dust across the Atlantic and
823 its impact over the Amazon Basin, *Atmospheric Chemistry and Physics*, 23, 9993–10014, doi:10.5194/acp-23-
824 9993-2023, 2023.

825 Washington, R., Todd, M. C., Lizcano, G., Tegen, I., Flamant, C., Koren, I., Ginoux, P., Engelstaedter, S., Bristow, C.
826 S., Zender, C. S., Goudie, A. S., Warren, A., and Prospero, J. M.: Links between topography, wind, deflation,
827 lakes and dust: The case of the Bodélé Depression, Chad, *Geophysical Research Letters*, 33,
828 doi:10.1029/2006gl025827, 2006.

829 Webb, N. P., LeGrand, S. L., Cooper, B. F., Courtright, E. M., Edwards, B. L., Felt, C., Van Zee, J. W., and Ziegler,
830 N. P.: Size Distribution of Mineral Dust Emissions From Sparsely Vegetated and Supply-Limited Dryland Soils,
831 *Journal of Geophysical Research: Atmospheres*, 126, doi:10.1029/2021jd035478, 2021.

832 Yamaguchi, N., Ichijo, T., Sakotani, A., Baba, T., and Nasu, M.: Global dispersion of bacterial cells on Asian dust, *Sci
833 Rep*, 2, 525, doi:10.1038/srep00525, 2012.

834 Zeileis, A. and Hothorn, T.: Diagnostic Checking in Regression Relationships, *R News*, 2, 7–10, 2002.

835 Zhang, B., Zhang, Y., and Jiang, X.: Feature selection for global tropospheric ozone prediction based on the BO-
836 XGBoost-RFE algorithm, *Scientific Reports*, 12, 9244, doi:10.1038/s41598-022-13498-2, 2022.

837 Zhuang, J., Dussin, R., Huard, D., Bourgault, P., Banihirwe, A., Raynaud, S., Malevich, B., Schupfner, M., Filipe,
838 Levang, S., Jüling, A., Almansi, M., RichardScottOz, RondeauG, Rasp, S., Smith, T. J., Stachelek, J., Plough,
839 M., Pierre, Bell, R., and Li, X.: pangeo-data/xESMF: v0.7.1 (v0.7.1), Zenodo [code],
840 doi:10.5281/zenodo.7800141, 2023.